Materials Advances

ROYAL SOCIETY OF CHEMISTRY

PAPER

View Article Online
View Journal | View Issue

Cite this: *Mater. Adv.*, 2021, **2**, 1378

Defect clustering in an Eu-doped $NaMgF_3$ compound and its influence on luminescent properties†

Afranio Sousa, [a] Adelmo Souza [b] and Heveson Lima *[c]

Luminescent properties of compounds based on lanthanide ions are strongly influenced by defect clustering, and unfortunately, these defects are not fully understood in lanthanide-doped fluoroperovskite materials. In this context, we studied the structural properties and effects upon incorporation of divalent and trivalent Europium dopant ions in the orthorhombic phase of $NaMgF_3$, combining classic atomistic simulations and crystal field models. We developed a new set of interatomic potentials that reproduce the structural properties, as well as lattice parameters, interatomic distances and volumes, and elastic properties, with good accordance with experimental results. Analysis of the solution energy revealed that Eu^{3+} is most energetically favourable in the Mg site, while Eu^{2+} is most favourable in the Na site. The mechanism of charge compensation was investigated in both cases. We also analysed the local symmetry, charge transfer in Eu–F chemical bonding, crystal field parameters, and $^7F_1$ energy sub-levels of the Eu^{3+} ion in the host matrix based on crystal field and electronegativity models. In addition, we discussed the photoionization cross-section and optically stimulated luminescence (OSL) decay pattern for Eu^{2+}-doped $NaMgF_3$. Thus, this work provides direction for new material design and opens up a framework to analyse structural and defect changes of fluroperovskite compounds upon lanthanide ion insertion.

Received 4th December 2020,
Accepted 25th January 2021

DOI: 10.1039/d0ma00953a

rsc.li/materials-advances

1 Introduction

Perovskite compounds are a class of special materials that have attracted wide attention in recent years for interesting applications, such as magnetoelectrics,[1,2] photovoltaics devices,[3–6] light-emitting diodes,[7,8] lasers,[9,10] photocatalysis,[11] memristors,[12] and ionizing radiation detectors.[13–15] Fluoroperovskite materials, ABF_3 (where A and B stand for alkali and alkaline earth metals, respectively), are a sub-class of perovskite compounds. In particular, $NaMgF_3$ is a material inserted in this family, with interesting properties related to optics and ionizing radiation dosimetry.[16,17] Rare earth-doped $NaMgF_3$ compounds have been considered promising materials for personal dosimetry because of the effective atomic number, similar to human tissue, and high sensitivity at low dosages.[18,19] Unlike the other materials of this class, such as $AMgF_3$ (A = Rb, K, and Cs), $NaMgF_3$ presents an orthorhombic perovskite structure with space group Pbnm at room temperature and standard pressure.[20]

Luminescent properties of $NaMgF_3$ nanoparticles doped with lanthanide ions and Mn, synthesized using a reverse micro-emulsion method, have been reported.[21,22] Furthermore, lanthanide ions doped into $NaMgF_3$ polycrystalline samples have also been prepared by the conventional solid-state reaction method.[23,24] In fact, lanthanide incorporation in compounds has been largely used to enhance luminescent properties. In particular, Eu^{3+}-doped materials are a well-known red emitting phosphors, widely used as spectroscopic probes because of their unique emission characteristics.[25–27] Valuable characterization information, such as local symmetry of the optically active ion, occupancy number, and Stark levels, can be obtained from emission characteristics of the Eu^{3+} ion. However, in many cases, the Eu ion is incorporated in a host matrix and aliovalent substitution occurs. The difference between the ionic radii of both ions (doped and host) is an important factor in evaluating the influence of aliovalent substitution, giving rise to material defects. Identifying these defects is crucial to accurately describing the spectroscopic properties and understanding specific mechanisms relevant to their application in optics and ionizing radiation detectors. Mechanisms of charge compensation are not yet established for Eu^{3+}- and Eu^{2+}-doped $NaMgF_3$. Some reports have suggested

[a] *Departamento de Física, Universidade Federal de Sergipe, 49100-000, São Cristóvão, SE, Brazil*
[b] *Centro Multidisciplinar do Campus de Bom Jesus da Lapa, Universidade Federal do Oeste da Bahia, 47600-000, Bom Jesus da Lapa, BA, Brazil*
[c] *Centro Multidisciplinar do Campus de Luís Eduardo Magalhães, Universidade Federal do Oeste da Bahia, 47850-000, Luís Eduardo Magalhães, BA, Brazil. E-mail: heveson.matos@ufob.edu.br*

† Electronic supplementary information (ESI) available. See DOI: 10.1039/d0ma00953a

different types of charge compensation in materials of the same family ($KMgF_3$[28–30] and $RbMgF_3$[31]) doped with different lanthanide ions. However, these discussions are based on ion sizes (doped and host), ignoring discussions about lattice solution energy. In addition, the symmetry site and coordination number of the optically active ion are not clear, as well as the substitution site in the host matrix. The optically stimulated luminescence (OSL) decay pattern and high sensibility of the $NaMgF_3$:Eu^{2+} compound for low dose levels are not fully established. Therefore, a systematic study is necessary to make predictions about the incorporation of defects in the $NaMgF_3$ structure.

Classical atomistic simulation is a reliable tool for modelling a range of ionic materials and to help understand theoretical and experimental results. In this methodology, interactions between atoms are determined by interatomic potentials that are essential to studying physical properties of the simulated systems. Several studies have been widely used to examine structural, mechanical, elastic, and dielectric properties in solid-state materials.[32–36] Furthermore, atomistic simulation is able to perform studies on defect properties with low computational cost, compared with other methodologies, and has been successfully employed to study defects.[37–40] In addition, atomistic simulation procedures, combined with crystal field theory, is an practical method for describing spectroscopic properties of lanthanide ion-doped compounds and their dopant-related effects. Recently, Otsuka *et al.*[41] performed a study from a spectroscopic point of view, combining atomistic simulation, the simple overlap model (SOM),[42] and the method of nearest neighbours[43] (theoretical models of crystal field). The combination of both methodologies successfully described local symmetry and coordination number of the optically active ion, crystal field parameters, crystal field strength, $^7F_1$ stark sub-levels, and splitting.

Thus, in this work, we used a combination of classic atomistic simulation-based ionic models and crystal field models to study the orthorhombic phase of $NaMgF_3$. Firstly, atomistic simulation was used to describe structural properties and the defect formation process with the incorporation of Eu^{3+} and Eu^{2+} ions into $NaMgF_3$. For this, we developed a new set of interatomic potentials to describe the interactions between ions for the compound in the orthorhombic phase and performed a study of the structural and elastic properties. We carried out a defect study to obtain the most favourable charge compensation mechanism. Secondly, crystal field models were used to study spectroscopic properties of Eu^{2+} and Eu^{3+} ion-doped $NaMgF_3$. Detailed local geometry of the optically active ion in this host matrix was obtained. In addition, photoionization cross-section calculations, associated with the first-order kinetic model, gave us information about the OSL decay pattern and high sensibility of the Eu^{2+}-doped $NaMgF_3$ compound.

2 Methodologies

2.1 Computational simulation

The atomistic simulation technique was used to study the perfect structure and defective lattice of orthorhombic $NaMgF_3$, performed by GULP code.[44] Relaxation of the lattice parameters and atomic positions was completed to find the lowest energy. A description of the structural properties of the system depends on a set of potential parameters, adopted for a reliable description of fundamental interactions between the ions. Long-range interactions were calculated by Coulomb potential and short-range interactions by Buckingham potential. Eqn (1) shows the representation of repulsive (or Pauli repulsion) and attractive (or van der Waals interaction) terms of the Buckingham potential:

$$V(r) = A\exp\left(-\frac{r}{\rho}\right) - \frac{C}{r^6} \quad (1)$$

where A, ρ, and C are parameters obtained by a fitting procedure, and r is interatomic distance between ions.

In addition, a model for efficient treatment of ionic polarization effects is necessary, and a simple model, known as the shell model,[45] was used. Ions in this model are represented by a core (massive, includes the nucleus plus core electrons) and shell (massless, includes valence electrons) connected by a harmonic constant. The formal charge of the ion is obtained by the sum of the core and shell charges.

The defect calculation was performed using a two-region strategy.[46] This method is very useful for calculating defects in atomistic simulations and has been used successfully.[47–51] The crystal lattice is divided into two spherical regions (I and II), where the defect (or defect cluster) is placed in the centre of these regions. The inner region I is the portion of the crystal located around the defect, allowing explicit relaxation of all the ion positions under the action of a force field. Region II is more distant from the defect and can be treated using an approximate continuous method, since ions in this region exhibit an interatomic displacement smaller than the ions in region I. To obtain reliable results, a convergence test, with an appropriate radius for these regions, is necessary. In this work, we used 12 and 18 Å for regions I and II, respectively. This corresponds to approximately 1000 ions in the region I and 2400 ions in region II. The total energy (E_T) can be calculated by the expression $E_T = E_1(x) + E_{12}(x,u) + E_2(u)$, where $E_1(x)$ is the energy of region I, $E_2(u)$ is the energy of region II, and $E_{12}(x,u)$ is the energy of the interaction region between them.

2.2 Crystal field parameters and Stark levels of the $^7F_1$ multiplet

Interaction between the lanthanide ion and its nearest neighbours (NNs) has been a discussion theme in research groups that work with lanthanide spectroscopy, for a long time. The point charge electrostatic model (PCEM)[52] was the first non-parametric model to discuss crystal field parameters from a theoretical point of view. The PCEM considers that the bond between the lanthanide ion and its chemical surrounding is purely ionic, where the charge factor is equal to ligand valence and is located at the NN's position. Although some considerations of the PCEM have led to unsatisfactory results from a quantitative point of view, it has been the base model for the development of other theoretical models.

The simple overlap model[42] used in our predictions is a theoretical model based on the PCEM, which has been largely used in lanthanide spectroscopy with satisfactory predictions.[53,54] The SOM introduces a small covalent character to describe Ln–NN chemical bonding. In this assumption, the effective interaction charge is defined as $-\rho_j g_j e$ and is located around the Ln–NN middle distance ($R_j/2\beta$). g_j is the charge factor devoted to Ln–NN chemical bonding, R_j is j-th NN distance from the Ln ion, e is the elementary charge, and $\beta_j = 1/(1 \pm \rho_j)$ is a factor that determines the position of the effective charge in the middle distance. The minus sign is applied when the charge is closer to the Ln ion, and the plus sign is applied when the charge is closer to the ligand. $\rho_j = \rho_0(R_0/R_j)^{3.5}$ describes the overlap of interacting wavefunctions, where R_0 is the smaller Ln–NN distance, and $\rho_0 = 0.05$ is the maximum overlap between the 4f and 2s (or 2p) orbitals.[55]

Through these considerations, the crystal field parameters (B_q^k) of the SOM can be related to PCEM, as show eqn (2):

$$B_q^k(\mathrm{SOM}) = \rho_j \left(\frac{2}{1-\rho_j}\right)^{k+1} B_q^k(\mathrm{PCEM}) \quad (2)$$

The $^7F_1$ energy sublevels of Eu^{3+} can be obtained through diagonalization of the crystal field matrix within the $^7F_1$ manifold.[56] Thus,

$$E_0 = \frac{2\sqrt{14}}{15} U^2 B_0^2 \quad (3)$$

$$E_- = \frac{-\sqrt{14}}{15} U^2 B_0{}^2 + \frac{7\sqrt{2}}{5\sqrt{3}} U^2 B_2{}^2 \quad (4)$$

$$E_+ = \frac{-\sqrt{14}}{15} U^2 B_0{}^2 - \frac{7\sqrt{2}}{5\sqrt{3}} U^2 B_2{}^2 \quad (5)$$

where E_0, E_-, and E_+ are energy sublevels for $J = 1$, measured in relation to the barycentre. U^2 is the reduced matrix element.[56]

2.3 Photoionization cross-section of trap levels

The photoionization cross-section (σ) is an essential quantity to understand the interaction processes of electromagnetic radiation with matter. Recently, Lima–Batista–Couto[57] proposed a model to obtain σ of localized traps in the band gap with activation energy E_i with respect to the conduction band, based on time-dependent perturbation theory. The model describes the trap level by a three-dimensional isotropic harmonic oscillator wavefunction with angular frequency ω_0, and the electron in the conduction band is described by the plane wavefunction. Following the same steps reported previously[57] and using the Fermi's golden rule, we obtain:

$$\sigma = \frac{4\alpha\hbar^2}{m^{*2}\omega\omega_0}\sqrt{\frac{\pi\hbar}{m^*\omega_0}}\exp\left\{-\frac{\hbar}{m^*\omega_0}\left[k^2 + \left(\frac{\omega}{c}\right)^2\right]\right\} \times 4\pi\left(\frac{1}{\gamma(\omega)}\right)^3 [\gamma(\omega)\cosh\cosh(\gamma(\omega)) - \sinh\sinh(\gamma(\omega))] \quad (6)$$

where $\gamma(\omega) = 2k\hbar\omega/m^*\omega_0 c$ is an energy function, ω is the angular frequency of incident electromagnetic radiation, m^* is the electron effective mass, α is the fine structure constant, $\hbar$ is Planck's reduced constant, c is the speed of light, and k is the wavevector of the electron. This expression is obtained considering all multipole terms in the Hamiltonian that couple the linear moment of the electron with the radiation electromagnetic field. This model was applied successfully to predict σ in promising materials for personal dosimetry and explain the mechanism of electron de-trapping with light stimulation.[57,58]

3 Results and discussion

3.1 Interatomic potentials of $NaMgF_3$

To analyse the structural properties and influence of defect clustering on the luminescent properties of the compound, describing the interactions between ions of the materials through a reliable set of interatomic potentials is necessary. We developed a new set of interatomic potentials for the orthorhombic phase of $NaMgF_3$ from an empirical fitting procedure, carried out with GULP code.[44] The empirical fitting was used to obtain Buckingham potential parameters for the Na–F interaction. The potential parameters used for Mg–F and F–F interactions were taken from a previous study[33] and have already been tested and validated for compounds of the same family, $AMgF_3$ (A = K, Cs, and Rb). Table 1 shows the interatomic potentials and shell model parameters used in all calculations of this work. A short range potential cutoff of 12 Å was used.

This set of interatomic potentials was validated, and the calculated lattice parameters of the $NaMgF_3$ compound are in excellent agreement with X-ray diffraction values, as well as mechanical properties. Elastic and dielectric constants are close to experimental values (see next section). The fluoride precursors NaF and MgF_2 are commonly used to synthesize $NaMgF_3$. In addition, the same set of potentials is also capable of modelling precursor fluorides (NaF and MgF_2). Even though the focus of this work was to analyse the orthorhombic $NaMgF_3$ phase, we were able to show that this set of interatomic potentials is transferable to the cubic phase of $NaMgF_3$, as well.

Table 1 Buckingham potential and shell parameters for $NaMgF_3$

Interaction	A (eV)	ρ (Å)	C (eV Å^6)	k (eV Å^{-2})	Y (e)	Ref.
Na^+_{core}–F^-_{shell}	1223.35	0.2682	0	—	—	This work
Mg^{2+}_{core}–F^-_{shell}	904.7	0.2825	0	—	—	Ref. 33
F^-_{shell}–F^-_{shell}	5050.2	0.2189	4	15	−1.378	Ref. 33

Calculations of the various precursor fluoride properties and cubic $NaMgF_3$ are shown in the supporting information (see Tables S1–S7, ESI†). These facts are important validation characteristics for successfully calculating defect properties.

3.2 Structural properties of the orthorhombic $NaMgF_3$

Table 2 presents a comparison between calculated and experimental data from lattice parameters and cell volumes for orthorhombic $NaMgF_3$. A relative error of less than 0.82% was calculated for all lattice parameters and cell volumes with respect to X-ray diffraction data.[59] Table 3 shows the most relevant interatomic distances for orthorhombic $NaMgF_3$ calculated in this work compared to experimental data.[59] The distances presented a relative error below 3% in all cases. These results show that our atomistic simulation has good acceptance in the reproduction of $NaMgF_3$ structural properties. In addition, a similar relative error was observed for all properties studied for cubic $NaMgF_3$ using the same set of interatomic potentials, as shown in the supporting information.

Fig. 1 presents the orthorhombic $NaMgF_3$ phase with space group *Pbnm* calculated for this work. The structure contains four non-equivalent (Na, Mg, F1, and F2) atoms. Mg^{2+} ions are coordinated by six F atoms, organized into three pairs of Mg–F bonds with approximately the same distances (two pairs of Mg–F2 bonds are equatorials and one pair of Mg–F1 bonds is apical). The Na atom is coordinated by eight F atoms, with only two Na–F1 bonds, and almost all bond distances are between Na–F2. This compound presents a different structural behaviour at room temperature and pressure compared to other materials of the same family ($AMgF_3$, A = Cs, Rb, and K).[33]

The elastic constants (C_{11}, C_{22}, C_{12}, C_{13}, C_{23}, C_{33}, C_{44}, C_{55}, and C_{66}) of $NaMgF_3$ in the orthorhombic phase are shown in Table 4, and the values calculated in this work are compared with experimental data.[60] The elastic constants satisfy Born's criteria and prove its mechanical stability. The reproducibility of these properties validates the potentials and transferability, which is crucial for modelling physical properties under conditions different from the initial fitting procedure. The bulk modulus, shear modulus, static dielectric constant (ε_0), and high-frequency dielectric constant (ε_∞) for orthorhombic $NaMgF_3$ are also shown in Table 4. In addition, our results show excellent transferability of these potentials for cubic $NaMgF_3$ (see ESI†). Having successfully completed this first step, we next analysed defect properties and their influence on spectroscopic properties of $NaMgF_3$.

Table 2 Lattice parameters and cell volumes for orthorhombic $NaMgF_3$

Lattice parameters	Ref. 59	This work	%
a (Å)	5.360	5.404	0.82
b (Å)	5.488	5.473	−0.27
c (Å)	7.666	7.689	0.30
V (Å^3)	225.53	227.40	0.83

Table 3 Interatomic distances (in Å) for orthorhombic $NaMgF_3$

Distance	Ref. 59	This work	%
Na–F1($x1$)	2.322	2.322	0.00
Na–F2($x2$)	2.303	2.337	1.48
Na–F1($x1$)	2.416	2.474	2.40
Na–F2($x2$)	2.563	2.640	3.00
Na–F2($x2$)	2.710	2.710	0.00
Na–F1($x1$)	3.097	3.079	−0.58
Na–F1($x1$)	3.185	3.118	−2.09
Mg–F2($x2$)	1.981	1.974	−0.35
Mg–F1($x2$)	1.979	1.976	−0.15
Mg–F2($x2$)	1.989	1.977	−0.60

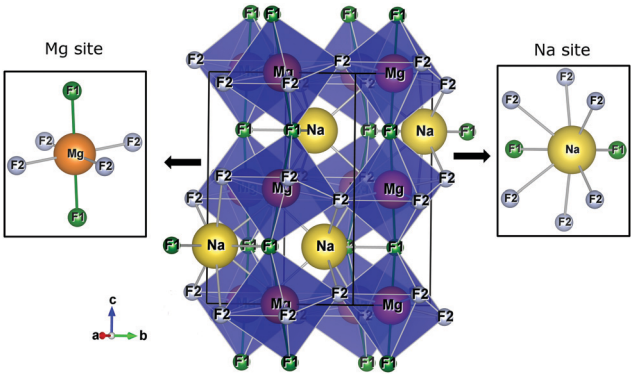

Fig. 1 The crystalline structure of $NaMgF_3$ in an orthorhombic lattice with space group *Pbnm*. Na and Mg sites are shown in detail.

Table 4 Elastic constants, bulk modulus, shear modulus and dielectric constants (static and high-frequency) for orthorhombic $NaMgF_3$

Elastic constants (GPa)	Ref. 60	This work	%
C_{11}	125.7	132.9	5.7
C_{22}	147.3	134.9	−8.4
C_{12}	49.5	50.2	1.4
C_{13}	45.1	46.2	2.4
C_{23}	43.1	47.8	10.9
C_{33}	142.5	135.1	−5.2
C_{44}	46.7	45.3	−3.0
C_{55}	44.8	43.4	−3.1
C_{66}	50.4	43.8	−13.1
Dielectric constants			
ε_0	—	7.75	—
ε_∞	—	2.20	—
Bulk modulus (GPa)	—	76.82	—
Shear modulus (GPa)	—	43.72	—

3.3 Defect calculations

The process of incorporating Eu^{3+} and Eu^{2+} ions into the $NaMgF_3$ compound requires a charge compensation mechanism to stabilize the local structure and accommodate extra charge in the relaxed structure. Interatomic potential used to describe Eu–F interactions was taken from a previous study for modelling natural apatite crystals,[61] and have already been tested and validated for Rare-Earth fluorides. The incorporation of defects into the crystalline structure, obtained by our

Table 5 Solid state reactions in the Kröger–Vink notation for Eu^{3+}-doped $NaMgF_3$

Schemes	Incorporating the Eu^{3+} into Na^+ site
(I)	$Na_{Na}^{\times} + EuF_3 \leftrightarrow Eu_{Na}^{\bullet\bullet} + 2F_i^{'} + NaF$
(II)	$Na_{Na}^{\times} + Mg_{Mg}^{\times} + EuF_3 \leftrightarrow Eu_{Na}^{\bullet\bullet} + V_{Mg}^{''} + NaMgF_3$
(III)	$3Na_{Na}^{\times} + EuF_3 \leftrightarrow Eu_{Na}^{\bullet\bullet} + 2V_{Na}^{'} + 3NaF$
(IV)	$Na_{Na}^{\times} + 2Mg_{Mg}^{\times} + NaF + EuF_3 \leftrightarrow Eu_{Na}^{\bullet\bullet} + 2Na_{Mg}^{'} + 2MgF_2$
(V)	$2Na_{Na}^{\times} + Mg_{Mg}^{\times} + 2EuF_3 \leftrightarrow 2Eu_{Na}^{\bullet\bullet} + V_{Mg}^{''} + 2F_i^{'} + NaF + NaMgF_3$
	Incorporating the Eu^{3+} into Mg^{2+} site
(VI)	$Mg_{Mg}^{\times} + EuF_3 \leftrightarrow Eu_{Mg}^{\bullet} + F_i^{'} + MgF_2$
(VII)	$Mg_{Mg}^{\times} + Na_{Na}^{\times} + EuF_3 \leftrightarrow Eu_{Mg}^{\bullet} + V_{Na}^{'} + NaMgF_3$
(VIII)	$3Mg_{Mg}^{\times} + 2EuF_3 \leftrightarrow 2Eu_{Mg}^{\bullet} + V_{Mg}^{''} + 3MgF_2$
(IX)	$2Mg_{Mg}^{\times} + NaF + EuF_3 \leftrightarrow Eu_{Mg}^{\bullet} + Na_{Mg}^{'} + 2MgF_2$
(X)	$2Mg_{Mg}^{\times} + Na_{Na}^{\times} + 2EuF_3 \leftrightarrow 2Eu_{Mg}^{\bullet} + Mg_{Na}^{\bullet} + 3F_i^{'} + NaMgF_3$
	Incorporating the Eu^{3+} into Na^+ and Mg^{2+} sites
(XI)	$Mg_{Mg}^{\times} + 3Na_{Na}^{\times} + 2EuF_3 \leftrightarrow Eu_{Mg}^{\bullet} + Eu_{Na}^{\bullet\bullet} + 2V_{Na}^{'} + F_i^{'} + 3NaF + MgF_2$
(XII)	$3Mg_{Mg}^{\times} + Na_{Na}^{\times} + 2EuF_3 \leftrightarrow Eu_{Mg}^{\bullet} + Eu_{Na}^{\bullet\bullet} + V_{Mg}^{''} + Na_{Mg}^{'} + 3MgF_2$

Table 6 Solid state reactions in the Kröger–Vink notation for Eu^{2+}-doped $NaMgF_3$

Schemes	Incorporating the Eu^{2+} into Na^+ site
(XIII)	$Na_{Na}^{\times} + EuF_2 \leftrightarrow Eu_{Na}^{\bullet} + F_i^{'} + NaF$
(XIV)	$2Na_{Na}^{\times} + Mg_{Mg}^{\times} + 2EuF_2 \leftrightarrow 2Eu_{Na}^{\bullet} + V_{Mg}^{''} + NaF + NaMgF_3$
(XV)	$2Na_{Na}^{\times} + EuF_2 \leftrightarrow Eu_{Na}^{\bullet} + V_{Na}^{'} + 2NaF$
(XVI)	$3Na_{Na}^{\times} + 2EuF_2 \leftrightarrow 2Eu_{Na}^{\bullet} + V_{Na}^{'} + F_i^{'} + 3NaF$
(XVII)	$Na_{Na}^{\times} + F_F^{\times} + EuF_2 \leftrightarrow Eu_{Na}^{\bullet} + V_F^{\bullet} + 2F_i^{'} + NaF$
(XVIII)	$Na_{Na}^{\times} + Mg_{Mg}^{\times} + EuF_2 \leftrightarrow Eu_{Na}^{\bullet} + Na_{Mg}^{'} + MgF_2$
(XIX)	$Na_{Na}^{\times} + Mg_{Mg}^{\times} + F_F^{\times} + EuF_2 \leftrightarrow Eu_{Na}^{\bullet} + V_{Mg}^{''} + V_F^{\bullet} + NaF + MgF_2$
(XX)	$3Na_{Na}^{\times} + F_F^{\times} + EuF_2 \leftrightarrow Eu_{Na}^{\bullet} + 2V_{Na}^{'} + V_F^{\bullet} + 3NaF$
	Incorporating the Eu^{2+} into Mg^{+2+} site
(XXI)	$Mg_{Mg}^{\times} + EuF_2 \leftrightarrow Eu_{Mg}^{\times} + MgF_2$

atomistic simulation, can estimate the preferred doping site and mechanism of charge compensation most favourably. Firstly, we consider the various possible schemes of charge compensation for the incorporation of Eu^{3+} and Eu^{2+} in the $NaMgF_3$ compound. Tables 5 and 6 show the proposed chemical reaction schemes, expressed in Kröger–Vink notation,[62] for the incorporation of Eu^{3+} and Eu^{2+} ions, respectively. After that, the next stage is the calculation of solution energy (E_{sol}) for each reaction, performed to predict the most energetically favourable scheme. The solution energy was obtained by a combination of defect energies, lattice energy of the fluoride precursor, and lattice energy of the dopant ion. In this work, the solution energies are calculated considering defects as isolated species (or unbound defects) and simulated in a cluster of defects (or bound defects). The motivation for calculating a cluster of defects is to account for the binding energy for different arrangements that frequently present the lowest energy. An example of how to calculate the solution energy for unbound ($E_{sol}^{unbound}$) or bound defects (E_{sol}^{bound}) is shown in eqn (7a) and (7b) for the first reaction (Scheme I) in Table 5. For the other reactions, a similar procedure is employed.

$$E_{sol}^{unbound} = E_{def}\left(Eu_{Na}^{\bullet\bullet}\right) + 2E_{def}\left(F_i^{'}\right) + E_{latt}(NaF) - E_{latt}(EuF_3) \quad (7a)$$

$$E_{sol}^{bound} = E_{def}\left(Eu_{Na}^{\bullet\bullet} + 2F_i^{'}\right) + E_{latt}(NaF) - E_{latt}(EuF_3) \quad (7b)$$

where E_{def} is the defect formation energy, and E_{latt} is lattice energy. More details regarding the calculation of solution energies are found in ref. 48.

Tables S8–S12 in the ESI† show defect and lattice energies required to perform the solution energy calculations.

Fig. 2 presents a solution energy diagram for bound and unbound defects for each reaction of Eu^{3+}-doped $NaMgF_3$, represented by schemes shown in Table 5. Notably, Eu^{3+} prefers to be incorporated into the Mg^{2+} site (E_{sol}^{bound} = 2.129 eV), compensated by a sodium vacancy (Scheme VII). Other reactions proposed here lead to values close to the red line. Reactions IV (entering into a Na^+ site) and VI (entering into a Mg^{2+} site),

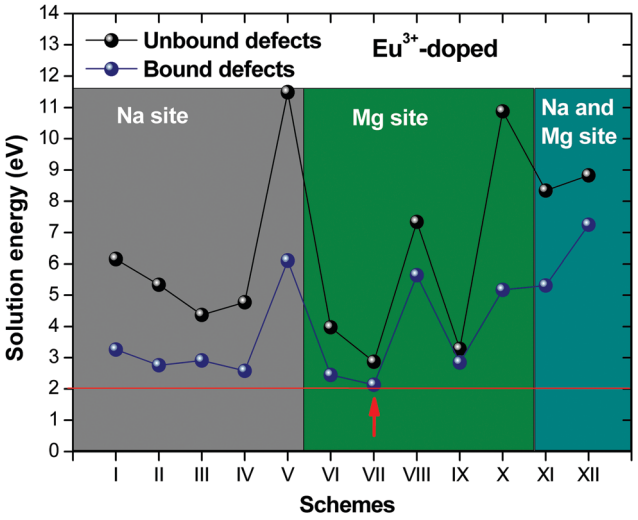

Fig. 2 Solution energies of bound and unbound defects for incorporation of Eu^{3+} into $NaMgF_3$.

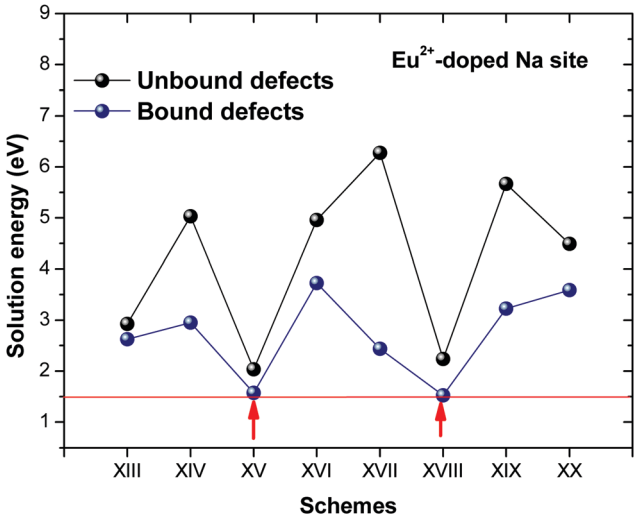

Fig. 3 Solution energies of bound and unbound for incorporation of Eu^{2+} into $NaMgF_3$.

for instance, have approximate differences of 0.5 and 0.3 eV, respectively, with respect to the lowest point. Our predictions show that mechanisms involving two substitutional defects in Na^+, Mg^{2+}, or both sites are practically unlikely in this configuration. In all cases, the calculations carried out in clusters lead to a decreased solution energy because of interactions between defects. Some reactions show considerable binding energy, leading to lower solution energy in comparison with unbound defect calculations.

In fact, the valence of ions is a determining factor for Eu^{3+} entering into the Mg^{2+} site instead of the Na^+ site. The ionic radius varies with coordination number, charge states, and other parameters.[63] Even though Eu^{3+} (0.947 Å for a coordination number of six) has a larger ionic radius than Mg^{2+} (0.72 Å for a coordination number of six) and is smaller than Na^+ (1.18 Å for a coordination number of eight), Eu^{3+} is preferable for replacing Mg^{2+} in the host matrix. In this case, the difference between the ionic radii of Eu^{3+} and Mg^{2+} ions are practically the same as Eu^{3+} and Na^+ ions. Thus, according to our calculations, the difference in valence between the Eu and Na ions leads to less favourable charge compensations for the system, even though the Eu^{3+} ion could be better accommodated by replacing the Na site instead of the Mg site.

Fig. 3 shows solution energy *versus* proposed charge compensation schemes (see Table 6) for incorporation of Eu^{2+} into the Na site of $NaMgF_3$. The most favourable mechanism of charge compensation is through the sodium vacancy (scheme XV) and anti-site (scheme XVIII), both with energy solutions of approximately 1.5 eV (see red arrow). Analyses of scheme XXI show (see Table 6, but not shown in Fig. 3), evidently, that the Eu^{2+}-doped Mg site requires no compensation mechanism because these ions have the same valence. The solution energy calculated for this scheme is approximately 2 eV. In other words, the calculations show that the Na site is energetically most favourable for the incorporation of the Eu^{2+} ion, rather than at the Mg site. In addition, our predictions show that the solution energy of bound defects is lower than unbound defects in all proposed schemes. These results show the importance of defect clustering in this system.

The most probable mechanism of Eu^{3+} and Eu^{2+} ion incorporation into $NaMgF_3$, charge compensation is illustrated in Fig. 4. Analysing the proposed chemical reactions and calculation of solution energies, we see that when calculations are carried out considering defects and the respective mechanism of charge compensation, as a defect cluster, the solution energy is less than when calculated as isolated defects. The configuration of the local site is modified in terms of distances and distortions. Understanding these changes is of great importance for a better understanding of luminescent properties of optically active ions in the host matrix.

Table 7 shows the interatomic distances (d) from the atomistic simulation after doping Eu^{3+} and Eu^{2+} ions into $NaMgF_3$ for the most favourable schemes found in this work. The percentage difference between Eu–F and Na–F (or Mg–F) interatomic distances is represented by Δ (%). The Na–F and Mg–F distances are taken from the pure $NaMgF_3$ phase (see Table 3) for comparison. We note that some distances are reduced, while others are increased for both cases (schemes) involving Eu^{2+}. For the cluster $\left(Eu^{\bullet}_{Na} + V'_{Na}\right)$, the atoms drastically approach Eu^{2+} with distances of less than 3 Å. For Eu^{3+}, in contrast with Eu^{2+}, all distances increase after doping. In this case, Δ (%) is around 10% for all interactions.

Experimental results based on photoluminescence spectra indicate that both Eu^{2+} and Eu^{3+} ions can co-exist in $NaMgF_3$, even although the emission spectrum from Eu^{3+} is quite different from the Eu^{2+} ion. In this case, when the $NaMgF_3$ is excited at 256 nm the emission from Eu^{2+} is observed at 366 nm, and when excited at 396 nm emission from Eu^{3+} at 590 nm is observed.[22] Although the Eu^{2+}/Eu^{3+} ratio depends on the chemical composition of the host,[64] the synthesis method[65] and exposure to ionizing radiation,[66,67] our calculations suggest that, from the perspective of solution energy, the Eu ion prefers to be incorporated into $NaMgF_3$ in its divalent state (see Fig. 2 and 3). Unlike Eu in the Na site, our calculations reveal that on the Mg^{2+} site, both Eu^{2+} and Eu^{3+} trivalent Europium are energetically favourable, once the energy difference is about

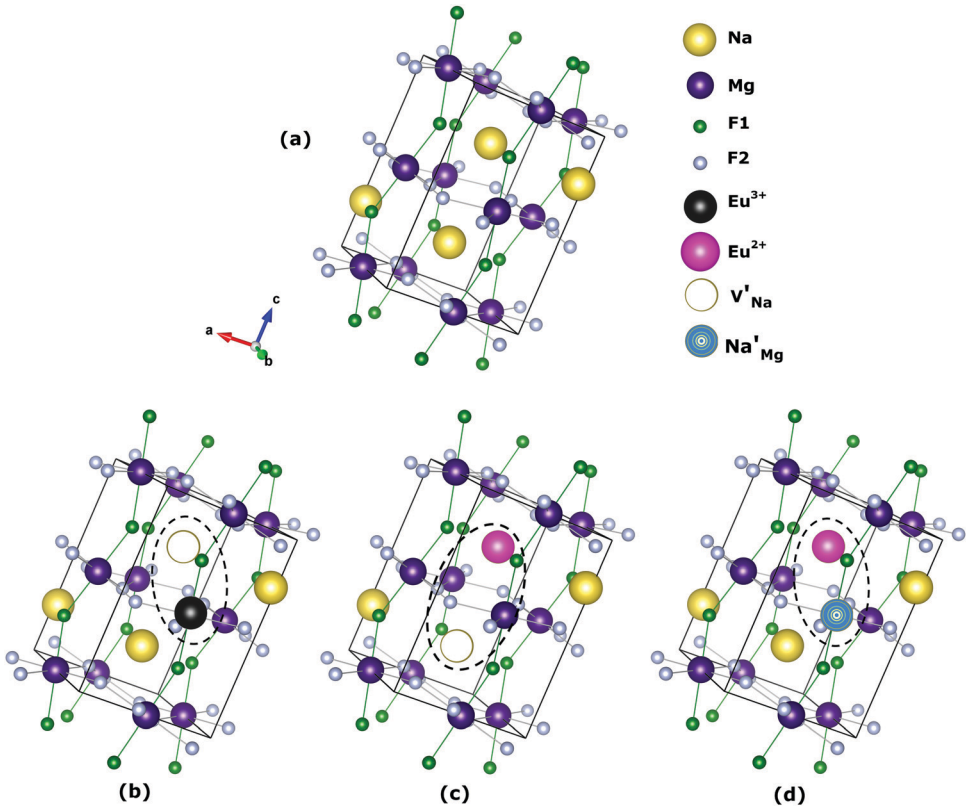

Fig. 4 Illustration of Eu^{3+} and Eu^{2+} incorporation into $NaMgF_3$ with the most favourable charge compensation mechanism: (a) pure $NaMgF_3$, (b) $\left(Eu^{\bullet}_{Mg} + V'_{Na}\right)$ cluster, (c) $\left(Eu^{\bullet}_{Na} + V'_{Na}\right)$ cluster, and (d) $\left(Eu^{\bullet}_{Na} + Na'_{Mg}\right)$ cluster.

Table 7 Comparison between interatomic distances (d in Å) of Eu^{2+} and Eu^{3+} ions doped in Na and Mg sites, considering the most favourable schemes

Eu^{2+} into Na site, $\left(Eu^{\bullet}_{Na} + V'_{Na}\right)$			Eu^{2+} into Na site, $\left(Eu^{\bullet}_{Na} + Na'_{Mg}\right)$			Eu^{3+} into Mg site, $\left(Eu^{\bullet}_{Mg} + V'_{Na}\right)$		
Eu–F	d (Å)	Δ (%)	Eu–F	d (Å)	Δ (%)	Eu–F	d (Å)	Δ (%)
Eu–F2	2.436	4.2	Eu–F2	2.467	5.6	Eu–F2	2.163	9.4
Eu–F2	2.436	4.2	Eu–F2	2.479	6.1	Eu–F2	2.197	11.1
Eu–F1	2.458	5.9	Eu–F1	2.463	6.1	Eu–F1	2.205	11.6
Eu–F1	2.592	4.8	Eu–F1	2.486	0.5	Eu–F1	2.161	9.4
Eu–F2	2.672	−1.4	Eu–F2	2.532	−6.6	Eu–F2	2.201	11.5
Eu–F2	2.672	−1.4	Eu–F2	2.727	0.6	Eu–F2	2.168	9.8
Eu–F2	2.633	−0.3	Eu–F2	2.533	−4.1			
Eu–F2	2.633	−0.3	Eu–F2	2.632	−0.3			
Eu–F1	2.715	−11.8	Eu–F1	2.911	−5.5			
Eu–F1	2.936	−5.8	Eu–F1	3.121	0.1			

0.133 eV. Thus, Eu^{2+} emission can arise from Eu localized in the Na and Mg sites. In fact, experimental results show that Eu^{2+} is dominant at lower concentrations, but Eu^{3+} becomes important when concentration increases. This behaviour is similar to that reported for Eu^{3+} and Eu^{2+} in CaF_2:Eu crystals.[68]

3.4 Spectroscopic properties of Eu ions in $NaMgF_3$

3.4.1 Local structure of the Eu^{3+} ion. In order to analyse the local symmetry and charges transferred in Eu–F chemical bonding and to calculate the crystal field parameters and Stark levels from the $^7F_1$ multiplet, relaxed positions of Eu^{3+} and its NNs are necessary. These positions are obtained from the most favourable mechanism of atomistic simulation presented in Section 3.3. In scheme VII, the most energetically favourable, Eu^{3+} has the same coordination number (six NNs) when incorporated into the Mg^{2+} site.

Spherical coordinates of the Eu^{3+} ion, obtained by atomistic simulations of defect clustering, are shown in Table 8. In dealing with a distorted structure, all Eu–F distances are slightly different and, consequently, symmetry discussions here are approximate.

We chose the principal axis of symmetry (z'-axis) by diagonalizing the tensor of the quadrupolar field, which is experienced by the optically active ion. In this case, the eigenvector

Table 8 Spherical coordinates with respect to the main axis of symmetry, with the Eu^{3+} ion at the origin of the system

Spherical coordinates[a]						
	Distorted S_6			Ideal S_6		
NN	R	θ	ϕ	R	θ	ϕ
F1	2.168	63.36	0	2.345	62.81	0
F2	2.161	60.77	240.83	2.345	62.81	240
F3	2.163	62.61	121.50	2.345	62.81	120
F4	2.197	128.30	302.49	2.345	117.19	300
F5	2.201	127.65	180.74	2.345	117.19	180
F6	2.205	130.11	61.56	2.345	117.19	60

[a] The ideal S_6 point symmetry corresponds to one site of Eu^{3+} in C-rare earth sesquioxides, taken from ref. 69, for comparison. The radial coordinates are given in angstroms, and the angular coordinates are given in degrees. The centroid (F1, F2, F3) coming out of the x'–y' plane is taken as the z'-axis.

takes the highest eigenvalues. The centroid (coming out the x'–y' plane) between the F1, F2, and F3 atoms is taken as the z'-axis to measure the spherical coordinates.

F1, F2, and F3 have slightly different distances, as well as F4, F5, and F6 atoms. The C_3 symmetry operation about the z'-axis takes, approximately, F2 to F1 and F1 to F3. Similarly, the atoms in the lower plane bounce off each other. Then, F1, F2, and F3 are approximately equivalent to each other. Likewise, F4, F5, and F6 may be considered approximately equivalent. This procedure reduces the degree of freedom in crystal field calculations by employing the same charge factor to equivalent atoms. Thus, we have used the charge factor g_1 to yellow atoms and g_2 to orange atoms.

Atomistic simulation was used to better understand the true nature of the defects in $NaMgF_3$, giving us information about spatial coordinates of the Eu^{3+} ion, which is not easily obtained by X-ray diffraction because of the low concentration of the Eu ion in the host matrix. Notably, a C_3 symmetry operation (Fig. 5) following a σ_h operation (reflection plane that contains the x'–y' plane) takes the same structural pattern, approximately. The bond distances illustrated in Fig. 5 can be found in Table 8. A combination of C_3 and σ_h operations is termed S_6 symmetry in group theory.[56] In this case, a distorted S_6 point symmetry occurs because all distances are slightly different, and the angles differ from that of ideal S_6 symmetry. Once in S_6 point symmetry, the electric dipole 4f–4f transitions are forbidden, and the distorted S_6 symmetry explains the weak electric dipole 4f–4f transitions of Eu^{3+} observed in $NaMgF_3$.

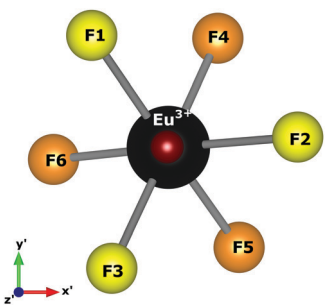

Fig. 5 Local symmetry of the optically active ion, and the axis adopted to obtain spherical coordinates. The centroid coming out the x'–y' plane is taken as the z'-axis.

Spectroscopic properties of Eu^{3+} in the Na sites must be quite different from Eu^{3+} substituting Mg^{2+}, due to low symmetry of the Na site. In addition, our simulation shows that there is also distortion when Eu^{2+} substitutes Na. This suggests that Eu^{2+} must be in a site with very low symmetry, which induces a high intensity 4f–4f transition. In fact, 4f–4f emission from Eu^{2+} in $NaMgF_3$ has intensity comparable with broad $4f^65d^1$–$4f^7$ emission, which is an allowed transition and occurs with a high transition probability. On the other hand, experimental results show that Eu^{3+} in low symmetry sites are less unlikely, and this has also been predicted in our simulations, showing that Eu^{3+} in a Na site is less probable.

3.4.2 Crystal field parameters. Table 9 shows charge factors and the set of crystal field parameters, B_q^k, for the distorted S_6 site. The B_q^k were calculated using spherical coordinates of Eu^{3+} ion incorporation into the Mn site of $NaMgF_3$ (Table 8), a set of charge factors (g_1 and g_2) that describes the interaction Eu–F in this dielectric medium, and the maximum overlap, ρ_0,

Table 9 Crystal field parameters (B_q^k in cm^{-1}) and charge factors[a] using β^- and β^+

B_q^k	β^-	β^+
B_0^2	−299.6	−299.53
B_1^2	$-8.144 - 27.578i$	$-7.555 - 26.408i$
B_2^2	22.523	22.225
B_0^4	−269.799	−211.583
B_1^4	$-0.98 - 8.615i$	$-1.118 - 6.937i$
B_2^4	$-20.045 - 8.944i$	$-16.209 - 6.732i$
B_3^4	$-50.207 + 522.044i$	$-28.773 + 416.689i$
B_4^4	$2.264 + 1.095i$	$1.657 + 1.034i$
B_0^6	413.269	272.774
B_1^6	$8.86 + 34.918i$	$6.044 + 22.983i$
B_2^6	$5.69i$	$0.049 + 3.418i$
B_3^6	$11.311–134.588i$	$5.575 - 93.281i$
B_4^6	$35.648–4.526i$	$22.963 - 3.444i$
B_5^6	$0.292 + 22.377i$	$0.333 + 14.947i$
B_6^6	$-282.947 - 53.841i$	$-187.929 - 25.489i$
g_1	0.435	0.58
g_2	0.034	0.031

[a] β^- and β^+ define the charge factor position around the middle distance of Eu–F. The minus signal means that g is closer to Eu^{3+}, and the plus sign indicates that g is closer to the ligands. A rotation (30.5°) about the principal axis was carried out to eliminate the imaginary part of B_2^2.

between 4f wavefunctions with ligand orbitals. In this case, we used the value ($\rho_0 = 0.05$) obtained by Axe and Burns.[55] Notably, all B_q^k are nonzero, as expected, because the local structure of the optically active ion is distorted. The B_q^k also allow for identification of Eu^{3+} ion symmetry, as well as predicting the $^7F_1$ state energy sublevels. In ideal S_6 symmetry,[56] only the following B_q^k values are nonzero: B_0^2, B_0^4, B_3^4, B_0^6, B_3^6, and B_6^6. We observe that the contribution of B_q^k values that represent S_6 symmetry are much higher than the others. B_1^2 and B_2^2 have approximately a 10% contribution in relation to B_0^2; B_1^4, B_2^4, and B_4^4 have a contribution around 4% in relation to B_0^4 and B_3^4. Likewise, B_1^6, B_2^6, B_4^6, and B_5^6 contribute approximately 10% in relation to B_0^6, B_3^6, and B_6^6.

This leads us to conclude that Eu^{3+} occupies is a distorted S_6 point symmetry. Furthermore, we have calculated B_q^k using β^- and β^+, which define the charge factor positions around the middle distance of Eu–F.[42] The minus signal means that g is closer to the Eu^{3+} ion, and the plus signal means that g is closer to the ligands. This parameter is a way (according to the SOM) to include covalence effects on the chemical bond because the charge is localized in a middle distance ($R/2\beta$) instead of being located at the position of the ligand, as proposed by the PCEM. In this case, the use of β^+ leads to a lower contribution from B_q^k that does not belong to ideal S_6 symmetry. In addition, the phenomenological charge factors, adjusted to reproduce the $^7F_1$ state energy sublevels, are higher.

We also use the model proposed by Lima *et al.*[70] to calculate charge transferred to the Eu–F chemical bond. This model is valid for high symmetry systems, in which only one charge factor is needed to describe the system. With ideal S_6 point symmetry, the model would be well applied, but for the sake of comparison, we have calculated one of the charges through this model using the following expression:

$$g = \Delta\chi(D)/R_{Eu-F} \quad (8)$$

where $\Delta\chi(D)$ is the Pauling electronegativity difference in Debye units ($D = 3.33 \times 10^{-30}$ C m), and R_{Eu-F} is the distance between the positive and negative charge centres. R_{Eu-F} can be obtained by the difference between the atomic and crystalline radii from the cations and anions (refer to ref. 71 for more information). By using benchmark values available in the publication by Shannon,[63] we find $R_{Eu-F} = 0.982$ Å. Thus, we obtain $g = 0.594$ using $\Delta\chi(D) = 2.8$. This value is closer to g_1 adjusted with β^+ (see Table 9).

The B_0^2 sign defines the position of the $^7F_1$ state ground sublevel from the barycentre. We see in Table 8 that it is correctly predicted using β^- and β^+ because B_0^2 is negative, and the $^7F_1$ state ground sublevel is non-degenerate. We will discuss this point in more detail in the next section.

3.4.3 $^7F_1$ state energy sublevels of the Eu^{3+} ion. Table 10 shows the experimental[22] and predicted $^7F_1$ state energy sublevels and splittings. The energy sublevels are measured with respect to the barycentre of the $^7F_1$ level. We use a set of phenomenological charge factors in the calculations of B_q^k to reproduce the energy sublevels and, consequently, the splitting. Our predictions were carried out using β^- and β^+ for comparison.

The photoluminescence emission spectra of $NaMgF_3$ nanoparticles containing Eu, excited at 396 nm, for 1% Eu show $^5D_0 \rightarrow {}^7F_J$ transitions from Eu^{3+}. The emission spectrum reported by Gaedtke and William[22] at room temperature presents one peak corresponding to the $^5D_0$–$^7F_0$ transition, two peaks from $^5D_0$–$^7F_1$, two peaks from $^5D_0$–$^7F_2$, and four peaks from $^5D_0$–$^7F_4$. $^5D_0$–$^7F_1$ is a magnetic dipole transition, which is not influenced by the crystalline environment. The number of lines and intensities in relation to the $^5D_0$–$^7F_2$ transition indicates if the system is lower or higher in symmetry. The other transitions are electric dipole moment transitions which are strongly influenced by the crystalline environment.

The second peak of the $^5D_0$–$^7F_1$ transition is doubly degenerate, and the $^7F_1$ splitting is less than 100 cm^{-1}. The emission spectrum reported by Gaedtke and William[22] shows that the $^5D_0$–$^7F_1$ transition is approximately 50% more intense than the $^5D_0$–$^7F_2$ transition. This suggests that the Eu^{3+} ion occupies point symmetry with a distorted inversion centre, although the emission spectrum shows peaks corresponding to the $^5D_0$–$^7F_0$ and $^5D_0$–$^7F_2$ transitions.

Schuyt and William,[24] based on the Tanner diagram,[72] suggested that the Eu^{3+} occupies sites with C_s, C_{nv} or C_n symmetry because the $^5D_0$–$^7F_0$ transition is presented in the emission spectrum. C_s is part of low symmetry groups, which is not the case here because the $^7F_1$ splitting is less than 350 cm^{-1} (ref. 73). Analysing the number of lines for each transition in the emission spectrum and comparing it with the Tanner diagram[72] indicates C_{3v} or C_{4v} symmetry. Previous work carried out with Eu^{3+}-doped $KMgF_3$ suggested the same symmetry.[28–30] However, C_{3v}, C_{4v}, and C_n are symmetry groups without inversion centres. The crystal field parameters related to the odd part of the crystal field potential is different from zero for this symmetry set (C_{3v}, C_{4v}, and C_n). In this case, the $^5D_0$–$^7F_2$ transition, allowed by electric dipole and strongly influenced by the environment, would be more intense than the transition $^5D_0$–$^7F_1$. This is not observed in the $NaMgF_3$:Eu emission spectrum. Thus, the most probable symmetry is distorted S_6 point symmetry. Due to distortion in the luminescent site, other transitions, beyond $^5D_0$–$^7F_1$, are apparent in the emission spectrum beyond transition.

E_{-1} and E_{+1} are slightly different because B_2^2 is nonzero. The distortion in S_6 point symmetry leads to a small contribution of this parameter in relation to B_0^2. This behaviour is not observed in the emission spectrum obtained experimentally. However, Seo *et al.*[28] showed a slight splitting of the second line around 0.7 nm in $KMgF_3$:Eu using site-selective laser-excitation

Table 10 Experimental[22] and predicted $^7F_1$ state energy sublevels and ΔE. The experimental energy sublevels with respect to the $^7F_0$ level are shown in parentheses. The other values are measured in relation to the barycentre

E (cm^{-1})	E_{exp}	$E(\beta^-)$	$E(\beta^+)$
E_0	−65.344 (315.689)	−58.674	−58.660
E_{-1}	32.672 (413.705)	19.230	19.357
E_{+1}	32.672 (413.705)	39.444	39.303
ΔE	98.016	98.118	97.963

spectroscopy. This agrees very well with our predictions because E_{-1} and E_{+1} are separated by approximately 20 cm^{-1}. In fact, the spectrometer used has a lower resolution, and a splitting of 0.7 nm cannot be identified in the emission spectrum.

Another point that deserves to be highlighted is the substitutional defect and charge compensation created by inserting Eu^{3+} into the host matrix. Reports for materials from the same family (Eu^{3+}-doped $KMgF_3$[28–30] and $RbMgF_3$[31]) have diverged in relation to substitutional defects and charge compensation. The reports for Eu-doped $KMgF_3$ have suggested a Na substitutional defect,[28–30] while one report for Eu-doped $RbMgF_3$ suggested an Mg substitutional defect.[31]

Our results for the Eu^{3+} ion in $NaMgF_3$ show a Mg substitutional defect compensated by a Na vacancy in the calculations with defect clustering (see Fig. 2, scheme VII). The energy difference of the most favourable mechanism for Eu^{3+} incorporation in Na and Mg sites is around 0.5 eV. Reaction (IV) in the Na site is less favourable; the local geometry of the optically active ion has a lower symmetry (with eight NNs) and higher distortion compared with the most favourable reaction. We tested this geometry in crystal field parameter calculations, but the predictions do not reproduce the emission spectrum characteristics through a set of positive charge factors. Moreover, values of B_q^k do not lead to any conclusion about the local symmetry of the Eu^{3+} ion (doped in the Na site). Thus, our conclusions are based on atomistic simulation, group theory, crystal field calculations, and emission spectrum characteristics of $NaMgF_3$:Eu. These results lead us to strongly believe that the Eu^{3+} ion is incorporated in the Mg site.

3.5 Photoionization cross-section and OSL decay pattern of $NaMgF_3:Eu^{2+}$

Polycrystalline $NaMgF_3:Eu^{2+}$ has been shown to be a suitable material for application in personal dosimetry. The material has high sensitivity and is able to monitor small doses, having a linear dose–response behaviour between μGy dose levels up to approximately 100 Gy.[18] However, this behaviour and the mechanism of electron de-trapping are not completely explained in the literature.

In this section, we discuss this point based on the photoionization cross-section (σ) of the trap level and associated it with the substitutional defect to understand the origin of the OSL signal from $NaMgF_3:Eu^{2+}$. We employed the model developed by Lima–Batista–Couto[57] to predict σ, and ref. 57 can be consulted for more details on the method.

Fig. 6 shows the photoionization cross-section as a function of the electromagnetic radiation energy for $NaMgF_3:Eu^{2+}$. The curve has a broad excitation interval that leads to electron de-trapping processes of localized traps in the band gap. OSL emission reported by Dotzler *et al.*,[18] excited at 450 nm, shows a broad interval of the emission spectra from samples pre-irradiated with X-rays. This agrees with our predictions. We also observe that the maximum peak occurs for light stimulus at approximately 2.2 eV, which corresponds to the maximum probability of electrons to be de-trapped from this localized trap.

We calculate the magnitude of σ to the specific wavelength, λ = 470 nm, which was the same wavelength used in the most

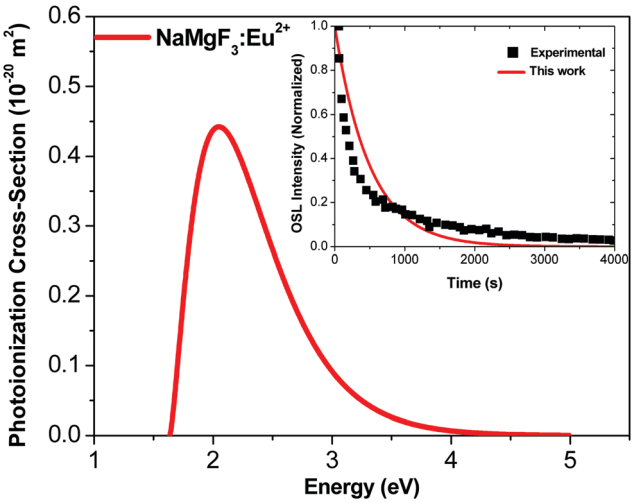

Fig. 6 Photoionization cross-section *versus* electromagnetic radiation energy for $NaMgF_3:Eu^{2+}$. Inset shows experimental data from ref. 77 and theoretical OSL decay patterns for $NaMgF_3:Eu^{2+}$. The experimental decay curve was obtained after irradiation with an X-ray dose of 219 mGy.[77]

OSL measurements. The phonon frequency used here is 325 cm^{-1}, obtained from ref. 74 $CaF_2:Yb^{2+}$. The electron effective mass used is $0.74m_e$, reported for fluoroperovskites in ref. 75. The activation energy used is 1.2 eV.[72] By using these values in eqn (6), we obtain $\sigma = 0.244 \times 10^{-20}$ m^2 for the $NaMgF_3:Eu^{2+}$ compound. This value is close to that obtained by Daniel *et al.*[76] for $NaMgF_3:Eu^{2+}$, Ce^{3+} using the fitting method of the linearly modulated (LM)-OSL experimental curve. There, the fitting curve was carried out with four components, and one value of σ was obtained for each component. The dominant term presents a magnitude of 0.112×10^{-20} m^2.

Using the value of σ calculated here, we estimate the OSL decay pattern of $NaMgF_3:Eu^{3+}$ based on the first-order kinetic approximation (no re-trapping), which assumes the OSL signal decay with stimulation time is due to de-trapping of captured electrons and subsequent radiative recombination. Fig. 6 (inset) shows the experimental and theoretical OSL decay patterns. The experimental OSL decay curve was obtained after irradiation with an X-ray dose of 219 mGy.[77] The decay time is slower than that exhibited in the commercial material, $Al_2O_3:C$.[58] We note that the theoretical curve deviates slightly from the experimental curve because the model used here is the first-order kinetic model.

The rate at which electrons captured in the trap are optically excited to the conduction band is proportional to σ, and the OSL decay pattern is governed by σ. Our predictions show that σ of $NaMgF_3$ is on the same order of magnitude (10^{-20} m^2) as the calculated value for $Al_2O_3:C$.[58] This explains the high sensibility when stimulated with blue light.

4 Conclusion

In summary, we combined classical atomistic simulation and crystal field models to describe the origin of defects and their

influence on luminescent properties of Eu-doped $NaMgF_3$ in the orthorhombic phase. We proposed a new set of interatomic potentials that reproduce the main properties of the orthorhombic phase. Defect calculations based on these interatomic potentials provide information regarding the energetic balance of dopant incorporation in this fluoroperovskite compound. In addition, using crystal field calculations, we explored, in detail, the type of defect and spectroscopic properties of the optically active ion. The main findings of this work are summarized below.

– The new set of interatomic potentials reproduced structural and elastic properties in the orthorhombic phase and precursor fluorides. In addition, the interatomic potential is transferable to the cubic phase, consistent with the literature.

– Defect calculations show that incorporation of Eu^{3+} ions into the Mg site, compensated by the Na vacancy, is the most energetically favourable. Further, the Eu^{2+} ion prefers to incorporate into the Na site, compensated by a Na vacancy or anti-site, in the host matrix. In addition, the solution energy with Eu^{2+} is lower than with Eu^{3+}.

– We predict the local symmetry and $^7F_1$ energy sub-levels of the Eu^{3+} ion by using the simple overlap model and the local geometry obtained in defect calculations.

– The weak intensity of the $^5D_0$–$^7F_2$ transition, as well as the small splitting of the second peak of the $^5D_0$–$^7F_1$ transition (observed in emission spectrum as doubly degenerate), occurs due to the distortion in S_6 local symmetry occupied by Eu^{3+} ions.

– Our predictions of the photoionization cross-section and OSL decay pattern show that $NaMgF_3$:Eu^{2+} presents a high sensibility for stimulus over a large range of wavelengths.

The new insights presented in this work show the importance of defect calculations, combined with crystal field and photoionization cross-section models, to successfully describe the luminescent properties of lanthanide-doped compounds.

Author contribution

Afranio Sousa: data curation, formal analysis, investigation, methodology, validation, writing – original draft, writing – review and editing. Adelmo Souza: visualization, investigation, data curation, writing – original draft. Heveson Lima: conceptualization, formal analysis, data curation, investigation, project administration, supervision, validation, visualization, writing – original draft, writing – review and editing.

Conflicts of interest

There are no conflicts to declare.

Acknowledgements

The authors acknowledge the CNPq (No. 441451/2019-5), CAPES and FAPESB/BA, Brazilian funding agencies for financial support.

References

1 M. Yang, A. Kc, A. C. Garcia-Castro, P. Borisov, E. Bousquet, D. Lederman, A. H. Romero and C. Cen, *Sci. Rep.*, 2017, **7**, 7182.
2 K. Miyata and X.-Y. Zhu, *Nat. Mater.*, 2018, **17**, 379–381.
3 M. Petrović, V. Chellappan and S. Ramakrishna, *Sol. Energy*, 2015, **122**, 678–699.
4 H. Liu, Z. Huang, S. Wei, L. Zheng, L. Xiao and Q. Gong, *Nanoscale*, 2016, **8**, 6209–6221.
5 H. J. Snaith, *Nat. Mater.*, 2018, **17**, 372–376.
6 W. Ke and M. G. Kanatzidis, *Nat. Commun.*, 2019, **10**, 965.
7 P. Meredith and A. Armin, *Nature*, 2018, **562**, 197–198.
8 Y. Wang, G. Ding, J.-Y. Mao, Y. Zhou and S.-T. Han, *Sci. Technol. Adv. Mater.*, 2020, **21**, 278–302.
9 A. Fu and P. Yang, *Nat. Mater.*, 2015, **14**, 557–558.
10 Z. Song, J. Zhao and Q. Liu, *Inorg. Chem. Front.*, 2019, **6**, 2969–3011.
11 K. Nie, H. Yang, Z. Gao and J. Wu, *Mater. Sci. Semicond. Process.*, 2018, **83**, 12–17.
12 X. Xiao, J. Hu, S. Tang, K. Yan, B. Gao, H. Chen and D. Zou, *Adv. Mater. Technol.*, 2020, **5**, 1900914.
13 D. J. Daniel, A. Raja, U. Madhusoodanan, O. Annalakshmi and P. Ramasamy, *Opt. Mater.*, 2016, **58**, 497–503.
14 H. Wei and J. Huang, *Nat. Commun.*, 2019, **10**, 1066.
15 A. Raja, R. Nagaraj, K. Ramachandran, V. Sivasubramani, G. Annadurai, D. Joseph Daniel and P. Ramasamy, *Mater. Sci. Eng., B*, 2020, **255**, 114531.
16 Y.-P. Du, Y.-W. Zhang, Z.-G. Yan, L.-D. Sun, S. Gao and C.-H. Yan, *Chem. – Asian J.*, 2007, **2**, 965–974.
17 J. J. Schuyt and G. V. M. Williams, *Radiat. Meas.*, 2020, **134**, 106326.
18 C. Dotzler, G. V. M. Williams, U. Rieser and A. Edgar, *Appl. Phys. Lett.*, 2007, **91**, 121910.
19 J. J. Schuyt, J. Donaldson, G. V. M. Williams and S. V. Chong, *J. Phys.: Condens. Matter*, 2020, **32**, 025703.
20 B. Lütgert and D. Babel, *Z. Anorg. Allg. Chem.*, 1992, **616**, 133–140.
21 G. V. M. Williams, S. Janssens, C. Gaedtke, S. G. Raymond and D. Clarke, *J. Lumin.*, 2013, **143**, 219–225.
22 C. Gaedtke and G. V. M. Williams, *Radiat. Meas.*, 2014, **71**, 258–261.
23 J. J. Schuyt and G. V. M. Williams, *Mater. Res. Bull.*, 2018, **106**, 455–458.
24 J. J. Schuyt and G. V. M. Williams, *J. Lumin.*, 2019, **211**, 413–417.
25 R. Pazik, J.-M. Nedelec and R. J. Wiglusz, *CrystEngComm*, 2014, **16**, 5308–5318.
26 K. Binnemans, *Coord. Chem. Rev.*, 2015, **295**, 1–45.
27 R. V. Perrella, C. S. N. Júnior, M. S. Góes, E. Pecoraro, M. A. Schiavon, C. O. Paiva-Santos, H. Lima, M. A. Couto dos Santos, S. J. L. Ribeiro and J. L. Ferrari, *Opt. Mater.*, 2016, **57**, 45–55.
28 H. J. Seo, T. Tsuboi and K. Jang, *Phys. Rev. B: Condens. Matter Mater. Phys.*, 2004, **70**, 205113.
29 V. S. Singh, C. P. Joshi, T. K. Gundu Rao and S. V. Moharil, *J. Alloys Compd.*, 2016, **657**, 848–854.

30 N. Pathak, S. Mukherjee, D. Das, D. Dutta, S. Dash and R. M. Kadam, *J. Mater. Chem. C*, 2020, **8**, 7149–7161.
31 A. Raja, G. Annadurai, D. J. Daniel and P. Ramasamy, *J. Alloys Compd.*, 2017, **727**, 215–223.
32 A. M. Sousa, A. F. Lima and M. V. dos S. Rezende, *J. Solid State Chem.*, 2019, **269**, 312–319.
33 A. Sousa and H. Lima, *J. Comput. Chem.*, 2020, **41**, 646–652.
34 N. J. Henson, A. K. Cheetham and J. D. Gale, *Chem. Mater.*, 1996, **8**, 664–670.
35 A. Walsh, C. R. A. Catlow, A. A. Sokol and S. M. Woodley, *Chem. Mater.*, 2009, **21**, 4962–4969.
36 K. T. Butler, *J. Mater. Chem. C*, 2018, **6**, 12045–12051.
37 A. M. Sousa, A. F. Lima and M. V. dos S. Rezende, *J. Alloys Compd.*, 2016, **689**, 977–982.
38 N. Kuganathan, S. Ganeshalingam and A. Chroneos, *Materials*, 2019, **12**, 2851.
39 E. Gonzalo, A. Kuhn, F. García-Alvarado and M. S. Islam, *J. Mater. Chem. A*, 2013, **1**, 6588.
40 Q. Hou, J. Buckeridge, T. Lazauskas, D. Mora-Fonz, A. A. Sokol, S. M. Woodley and C. R. A. Catlow, *J. Mater. Chem. C*, 2018, **6**, 12386–12395.
41 A. M. Otsuka, D. O. Junot, H. Lima, M. V. dos, S. Rezende and M. A. C. dos Santos, *J. Lumin.*, 2020, **226**, 117503.
42 O. L. Malta, *Chem. Phys. Lett.*, 1982, **88**, 353–356.
43 Y. A. R. Oliveira, H. Lima, A. S. Souza and M. A. Couto dos Santos, *Opt. Mater.*, 2014, **36**, 655–657.
44 J. D. Gale, *J. Chem. Soc., Faraday Trans.*, 1997, **93**, 629–637.
45 B. G. Dick and A. W. Overhauser, *Phys. Rev.*, 1958, **112**, 90–103.
46 N. F. Mott and M. J. Littleton, *Trans. Faraday Soc.*, 1938, **34**, 485.
47 G. Busker, A. Chroneos, R. W. Grimes and I.-W. Chen, *J. Am. Ceram. Soc.*, 2004, **82**, 1553–1559.
48 A. Corgne, N. L. Allan and B. J. Wood, *Phys. Earth Planet. Inter.*, 2003, **139**, 113–127.
49 J. A. Dawson, C. L. Freeman, J. H. Harding and D. C. Sinclair, *J. Solid State Chem.*, 2013, **200**, 310–316.
50 C. A. J. Fisher, V. M. Hart Prieto and M. S. Islam, *Chem. Mater.*, 2008, **20**, 5907–5915.
51 M. S. Islam, D. J. Driscoll, C. A. J. Fisher and P. R. Slater, *Chem. Mater.*, 2005, **17**, 5085–5092.
52 M. R. Kibler, *Int. J. Quantum Chem.*, 1975, **9**, 403–420.
53 P. Porcher, M. Couto Dos Santos and O. Malta, *Phys. Chem. Chem. Phys.*, 1999, **1**, 397–405.
54 H. Lima, H. C. C. de Oliveira, X. Bidault, T. S. dos Santos, S. Chaussedent and M. A. Couto dos Santos, *J. Non-Cryst. Solids*, 2016, **448**, 62–67.
55 J. D. Axe and G. Burns, *Phys. Rev.*, 1966, **152**, 331–340.
56 C. Görller-Walrand and K. Binnemans, in *Handbook on the Physics and Chemistry of Rare Earths*, Elsevier, 1996, vol. 23, pp. 121–283.
57 H. Lima, J. V. Batista and M. A. Couto dos Santos, *EPL*, 2016, **115**, 33002.
58 B. Novais, E. Ferraz, A. S. Souza, P. L. Antonio, L. V. E. Caldas, J. Batista and H. Lima, *Opt. Mater.*, 2020, **102**, 109792.
59 Y. Zhao, J. B. Parise, Y. Wang, K. Kusaba, M. T. Vaughan, D. J. Weidner, T. Kikegawa, J. Chen and O. Shimomura, *Am. Mineral.*, 1994, **79**, 615–621.
60 Y. Zhao and D. J. Weidner, *Phys. Chem. Miner.*, 1993, **20**, 419–424.
61 J. A. L. Rabone and N. H. De Leeuw, *J. Comput. Chem.*, 2006, **27**, 253–266.
62 F. A. Kröger and H. J. Vink, *Solid State Physics*, Elsevier, 1956, vol. 3, pp. 307–435.
63 R. D. Shannon, *Acta Crystallogr., Sect. A: Found. Crystallogr.*, 1976, **32**, 751–767.
64 H. Terraschke and C. Wickleder, *Chem. Rev.*, 2015, **115**, 11352–11378.
65 K. Biswas, A. D. Sontakke, R. Sen and K. Annapurna, *J. Fluoresc.*, 2012, **22**, 745–752.
66 V. N. Bapat, *J. Phys. C: Solid State Phys.*, 1977, **10**, L465–L467.
67 P. W. Levy, *Nucl. Tracks Radiat. Meas.*, 1985, **10**, 547–556.
68 H. Yu, B. Zhang, X. Chen, X. Qian, D. Jiang, Q. Wu, J. Wang, J. Xu and L. Su, *Opt. Express*, 2019, **27**, 523.
69 H. Kohlmann, C. Hein, R. Kautenburger, T. C. Hansen, C. Ritter and S. Doyle, *Z. Kristallogr. Cryst. Mater.*, 2016, **231**, 517–523.
70 H. Lima and M. A. Couto dos Santos, *J. Phys. Chem. Solids*, 2016, **96–97**, 38–41.
71 H. Lima, D. Ferreira, A. S. Souza and M. A. C. dos Santos, *J. Braz. Chem. Soc.*, 2021, **32**, 405–412.
72 P. A. Tanner, in *Lanthanide Luminescence*, ed. P. Hänninen and H. Härmä, Springer Berlin Heidelberg, Berlin, Heidelberg, 2010, vol. 7, pp. 183–233.
73 K. Binnemans and C. Görller-Walrand, *Chem. Phys. Lett.*, 1995, **245**, 75–78.
74 M. F. Reid, P. S. Senanayake, J.-P. R. Wells, G. Berden, A. Meijerink, A. J. Salkeld, C.-K. Duan and R. J. Reeves, *Phys. Rev. B: Condens. Matter Mater. Phys.*, 2011, **84**, 113110.
75 H. Benmhidi, H. Rached, D. Rached and M. Benkabou, *J. Electron. Mater.*, 2017, **46**, 2205–2210.
76 D. J. Daniel, O. Annalakshmi, U. Madhusoodanan and P. Ramasamy, *J. Rare Earths*, 2014, **32**, 496–500.
77 J. J. Schuyt and G. V. M. Williams, *Radiat. Meas.*, 2019, **121**, 99–102.